



Simulating the radiative forcing of oceanic dimethylsulfide (DMS) in Asia based on Machine learning estimates

Junri Zhao^{1,2}, Weichun Ma^{1,3}, Kelsey R Bilsback⁴, Jeffrey R Pierce⁴, Shengqian Zhou^{1,2}, Ying Chen^{1,2}, Guipeng Yang⁵, Yan Zhang^{1,2,3,6*}

- 5 ¹Shanghai Key Laboratory of Atmospheric Particle Pollution and Prevention (LAP3), Department of Environmental Science and Engineering, Fudan University, Shanghai 200438, China
²Shanghai Institute of Eco-Chongming (SIEC), Shanghai 200062, China
³Institute of Digitalized Sustainable Transformation, Big Data Institute, Fudan University, Shanghai 200433, China
⁴Department of Atmospheric Science, Colorado State University, Fort Collins, CO, United States of America
10 ⁵Key Laboratory of Marine Chemistry Theory and Technology, Ministry of Education, College of Chemistry and Chemical Engineering, Ocean University of China, Qingdao 266100, China
⁶National Observations and Research Station for Wetland Ecosystems of the Yangtze Estuary, Shanghai, China

Correspondence to: Yan Zhang (yan_zhang@fudan.edu.cn)

15 **Abstract.** DMS emitted from the sea water is a key precursor to new particle formation, acting as a regulator in Earth's warming climate system. However, DMS's effects are not well understood in various ocean regions. In this study, we estimated DMS emissions based on a machine learning method and used the GEOS-Chem global 3D chemical transport model coupled with the Two Moment Aerosol Sectional (TOMAS) microphysics scheme to simulate the atmospheric chemistry and radiative effects of DMS. The contributions of DMS to atmospheric SO₄²⁻ aerosol and cloud condensation nuclei (CCN) concentrations
20 along with their radiative effect over the Asian region were evaluated for the first time. Firstly, we constructed novel monthly-resolved DMS emissions (0.5° × 0.5°) for the year 2017 using a machine learning model. 4351 seawater DMS measurements (including the recent ones over the Chinese Sea) and 12 relevant environment parameters were selected for training. We found the model could predict the observed DMS concentrations with a correlation coefficient of 0.75 and fill the values in regions lack of observations. Across Asian Seas, the highest seasonal mean DMS concentration occurred in Mar-Apr-May (MAM),
25 and we estimate annual DMS emission flux of 1.25 Tg (S), which accounts for 15.4% of anthropogenic sulfur emissions over the entire simulation domain (covers most of Asia) in 2017. The model estimates of DMS and methane sulfonic acid (MSA), using updated DMS emissions, were evaluated by comparing with cruise survey experiments and long-term online measurement site data. The improvement in model performance can be observed compared with the global-database DMS emissions. The relative contributions of DMS to SO₄²⁻ and CCN were higher in remote oceanic areas, which reached up to 88%
30 and 42% of all sources. Correspondingly, the sulfate direct radiative forcing (DRF) and indirect radiative forcing (IRF) contributed by DMS ranged from -200 to -20 mW m⁻² and -900 to -100 mW m⁻², respectively, with levels varying by season. The strong negative IRF is mainly over remote ocean regions (-900 to -600 mW m⁻²). Generally, the magnitude of IRF derived



by DMS was twice as large as its DRF. This work provides insights into the source strength of DMS and its impact on climate, addressing knowledge gaps related to factors controlling aerosols in the marine boundary layer and their climate impacts.

35 1 Introduction

Ocean-emitted DMS is a precursor of non-sea-salt SO_4^{2-} and controls the composition, size distribution, and number concentrations of aerosols over the remote oceanic areas. SO_4^{2-} directly influences the climate system by reflecting solar radiation back into the space, and indirectly, acting as CCN and altering the albedo of clouds and changing cloud radiative properties (Andreae and Rosenfeld, 2008). The “CLAW” hypothesis proposed by Charlson et al. (1987) assumed that negative
40 feedback interactions between ocean plankton and climate system, where the Earth system acted to buffer itself from warming, was linked through DMS production. Thereafter, several studies found that significant impacts of DMS induced aerosols on CCN and cloud albedos in remote oceans (Park et al., 2017; Quinn et al., 2017; Kulmala et al., 2014; Vallina and Simó, 2007), which lend credence to CLAW hypothesis. Nevertheless, due to low sensitivity of each step of the interactions to changes in
45 force factors in the CLAW climate feedback loop (e.g., low sensitivity of DMS production to changes in incident solar radiation), Quinn and Bates (2011) disproved the hypothesis. Whether the CLAW climate feedback is positive or negative is still uncertain, and further research is need to quantify the climate effect of DMS.

Building an accurate emission inventory is key to simulating the climate effects of DMS. As many previous studies have shown (Chen et al., 2018; Hodshire et al., 2019; Rap et al., 2013; Yang et al., 2017; Zhao et al., 2021), the marine DMS emissions used in numerical models mainly were estimated using an interpolation scheme (Kettle et al., 1999; Lana et al., 2011), which
50 mostly estimated DMS climatology by interpolating observed DMS data in limited sites to the global ocean. At first, observations from Global Surface Seawater DMS Database were binned and grouped into 57 ecological geographic ocean provinces, with weighted interpolations from near provinces used to fill the values where without observations. Wang et al., (2020) has pointed out that there were uncertainties in using spatial and temporal averaged data to fill regions without observations. However, artificial neural networks can potentially be trained and used to fill measurement gaps (Wang et al.,
55 2020). Galí et al. (2018) created a remote sensing algorithm to estimate DMS concentrations which is based on the relationship between a precursor of DMS and plankton light exposure. Their results (Galí et al., 2018) indicated that the remote sensing algorithms have better ability to reproduce the climatological features of DMS seasonality than interpolated DMS climatologies, which also outweigh the disadvantage of the interpolation scheme used in previous study (Lana et al., 2011). In a recent study (Bell et al., 2021), long-term in-situ DMS measurements conducted in North Atlantic Ocean from 2015 to 2018
60 were compared with the interpolated DMS climatologies (Lana et al., 2011) and predicted DMS concentrations from the remote sensing algorithm (Galí et al., 2018) and the neural network approach (Wang et al., 2020), which revealed that that both the remote sensing algorithm and the neural network model reproduce the sea water DMS trends better than the interpolated climatologies. However, DMS predictions from two model (Galí et al., 2018; Wang et al., 2020) tend to be underpredicted, likely because the primary biological processes of DMS production was not accounted for (Bell et al., 2021).



65 There are several modelling studies which have quantified the aerosol direct and indirect radiative forcing of DMS on a
global scale. The global annual mean DMS aerosol indirect radiative forcing estimates have ranged from -6.55 to -0.23 W/m²
(Mahajan et al., 2015; Thomas et al., 2010; Rap et al., 2013; Yang et al., 2017; Jin et al., 2018). There have been few studies that
have reported the radiative effect of DMS on a regional scale. Choi et al. (2020) adopted an empirical algorithm to estimate
DMS concentrations and calculated direct radiative effect of DMS aerosol, that is -1.3 W/m² for the year 2014-2016 over East
70 Asian seas, which was even higher than those global results (Yang et al., 2017; Rap et al., 2013). And there were no evaluations
of the DMS predictions in the seawater and atmosphere in their studies, which leads to an unknown reliability of the results.
The annual-mean direct radiative forcing due to DMS produced aerosol were -0.2 to -0.1 W/m² over East Asia reported by Li
et al. (2019) who used a DMS climatology (Lana et al., 2011) with 1° × 1° horizontal resolution for radiative forcing calculation.
As mentioned before, some uncertainties in the DMS climatology estimated by an interpolation scheme and coarse grid (1° ×
75 1°) may not be appropriate for regional simulations. In the previous studies (Li et al., 2020b; Li et al., 2020a), we used long-
term DMS measurements in 2011, 2013, 2015, 2016, and 2017 from a series of shipboard field experiments and performed
interpolation to map DMS concentrations in Chinese seas. The newest DMS measurements were used to explore the impact
of DMS on air quality over coastal areas of China, but the radiative effect of DMS was not reported.

To our knowledge, this is the first systematic study of the Asia region that quantifies the impacts of DMS on sulfate,
80 particle number concentration, and radiative forcing by using state-of-the-art aerosol microphysics model coupled on global
3D chemical transport model. In this study, we first trained 12 environmental parameters and newly updated DMS
measurements by utilizing eXtreme Gradient Boosting (XGBoost) machine learning algorithms (Chen and Guestrin, 2016)
used to construct a new regional DMS emissions for the year 2017 with a plausible underlying basis in ocean environmental
parameters. Then, the model performances of DMS and MSA were evaluated by comparing the model simulations with
85 shipboard field measurements and long-term online measurement site data. Finally, the annual-average and seasonal impacts
of DMS on sulfate/CCN concentrations and direct/indirect radiative forcing were quantified.

2 Methods and data

2.1 GEOS-Chem-TOMAS

90 In this study, the GEOS-Chem version 12.9.3 (<https://doi.org/10.5281/zenodo.3974569>, last access: 25 March 2021) cou-
pled with the online TOMAS aerosol microphysics model (Adams and Seinfeld, 2002) was adopted to calculate atmospheric
aerosol size, number, and mass concentrations from marine DMS emissions. TOMAS was used to simulate aerosol microphy-
sics processes (i.e., nucleation, coagulation, condensation, cloud processing). The advantage of TOMAS is the full size resol-
ution for all chemical species and the conservation of aerosol number, which allows modeler to construct aerosol and CCN n-
95 umber budgets that will balance. GEOS-Chem-TOMAS (GC-TOMAS) has been used in a range of previous studies (Kodros
and Pierce, 2017; Pierce and Adams, 2006; Kodros et al., 2016; D'Andrea et al., 2013; Westervelt et al., 2013; Lee et al., 2009; T



100 rivitayanurak et al., 2008;Pierce et al., 2007;Adams and Seinfeld, 2002). The model contains detailed hydrocarbon – nitrogen
oxide (NO_x) – ozone (O_3) - volatile organic compounds (VOC) – bromine oxides (BrO_x) tropospheric chemistry (Bey et al., 20
01) and aerosol species (including sulfate, nitrate, ammonium, black carbon, organic carbon, mineral dust, and sea salt) (Dun
can Fairlie et al., 2007;Pye et al., 2009;Alexander et al., 2005;Park et al., 2004) that are fully coupled to gas-phase chemistry,
with the ISORROPIA II algorithm to calculate the thermodynamic equilibrium between aerosols and their gas phase precurs
ors (Fountoukis and Nenes, 2007). The model includes detailed wet and dry deposition scheme for aerosols and gas species w
hich have been described in previous studies (Wesely, 2007;Liu et al., 2001;Wang et al., 1998;Amos et al., 2012). This versio
n of GC-TOMAS tracks the total aerosol particle number and the mass of each aerosol species (sulfate, mineral dust, sea salt,
105 hydrophilic and hydrophobic organic carbon, externally and internally mixed elemental carbon, and aerosol water) across 15
logarithmically size bins ranging from 3 nm to 10 μm (Lee and Adams, 2012;Lee et al., 2013). Since the ammonium nitrate
size distribution is not explicitly tracked with GC-TOMAS, so we assume that it follows the aerosol water distribution(Bilsba
ck et al., 2020a;Bilsback et al., 2020b).

110 The simulation domain covers most of Asia (11°S to 55°N , 60 – 150°E), discretized with a horizontal grid resolution of 0.
 $5^\circ \times 0.625^\circ$ and 47 vertical layers, and uses Modern-Era Retrospective Analysis for Research and Applications Version (ME
RRA-2) assimilated meteorological field for meteorological inputs (Gelaro et al., 2017). To assess radiative impacts of DMS
emissions at a regional scale, we performed three different annual simulations for the year 2017 (Table 1). The XG simulatio
n represents DMS emissions were calculated from our updated DMS emissions estimates (see Section 2.3) and the other (LA
NA) refer to DMS emissions from Lana DMS climatology (Lana et al., 2011), which is default setting in current version of G
eos-Chem model. The ND simulation represents DMS emissions tuned off. Each simulation was conducted with 1 month spi
n-up period (December 2016). The boundary conditions for the simulation domain were obtained from global simulations at
115 $2^\circ \times 2.5^\circ$ with 47 vertical layers.

For anthropogenic emissions in Asia, we used the recently updated Global anthropogenic emission inventories ($0.5^\circ \times 0.$
 5°) or the year 2017 from the open-source Community Emissions Data System (CEDS) (McDuffie et al., 2020), which applie
120 d scale factors from Zheng et al., (2018) to update China's emissions for the year 2017. Since there is a significant reduction
(62%) in SO_2 emissions in China from 2010 to 2017 (Zheng et al., 2018), updated emissions for China are crucial for quantif
ying contributions of biogenic sulfur source over Asia. Biomass burning emissions in the GC-TOMAS are obtained from Glo
bal Fire Emissions Database Version 4 (van der Werf et al., 2017). Dust, biogenic VOCs, sea salt, soil NO_x , and lighting NO_x
emissions are calculated online based on MERRA-2 meteorological field. The Dust Entrainment and Deposition (DEAD) sc
125 heme from Zender et al., (2003) was implemented GEOS-Chem to simulate dust mobilization. The Model of Emissions of G
ases and Aerosols from Nature from Guenther et al., (2012) was used to generate biogenic VOCs emissions. Soil and lighting
 NO_x emissions are calculated by parameterization scheme described in Hudman et al., (2012) and Price and Rind (1992), res
pectively.

The sea-air flux of DMS is estimated using the following the empirical formula as described in (Lana et al., 2011):

130
$$F = C_w \times k_w \times (1 - \gamma) \quad (1)$$



Where, C_w is the seawater DMS concentrations and k_w is the water side gas transfer velocity and γ is the atmospheric g
radient fraction. In this study, we selected the Nightingale et al. (2000) parameterization (hereafter N00) for k_w to represent t
he DMS emissions over the global ocean.

135 2.2 Radiative forcing calculation scheme

To calculate the top-of-atmosphere (TOA) all sky DRF and cloud-albedo IRF, we used Rapid Radiative Transfer Model
for Global Climate Models (RRTMG) (Iacono et al., 2008) with monthly averaged aerosol number and mass concentrations
from GC-TOMAS output and meteorological variables from MERRA2. For the DRE, we calculated aerosol optical depth
(AOD) single scattering albedo, and the asymmetry parameter based on Mie theory (Bohren and Huffman, 1983) and refractive
140 indices from the Global Aerosol Database (Koepke et al., 1997). In all cases, the DRE was calculated for core-shell optical
assumption, where, for each aerosol size bin, black carbon was represented as a spherical core within a homogenous shell of
all other hydrophilic species. For the cloud-albedo IRF, we calculate cloud droplet number concentration (CDNC) using the
activation parameterization from Abdul-Razzak and Ghan (2002). Cloud-liquid water content is prescribed from MERRA-2
and held fixed, and hence we only calculated the cloud-albedo (Twomey) indirect effect. The changes in effective cloud drop
145 radii were estimated following the cloud-droplet-radius perturbation method used in previous studies (Rap et al., 2013;Kodros
et al., 2016;Scott et al., 2014). Then, RRTMG is used to calculate the changes of TOA radiative flux from the changes effect
cloud drop radii, and we limit this calculation to liquid clouds, which is a limitation in this method. More detailed information
about implementation of RRTMG in GC-TOMAS can be found in Kodros et al., (2016).

150 2.3 Machine learning estimates of sea-surface DMS concentration for calculating DMS emission flux

To better capture the nonlinear relationship between DMS and its influencing parameters, we trained XGBoost model
(machine learning algorithm under the Gradient Boosting framework) with the entire dataset to predict sea surface DMS
concentrations where without the observations. Figure S1 shows the spatial distribution of DMS measurements. The red points
(1022 valid measurements) represent local DMS observations dataset (2011, 2013, 2015, 2016, and 2017) in Chinese seas
155 from China Ocean University. Details can be found in our previous studies (Yang et al., 2015a;Yang et al., 2014;Yang et al.,
2015b;Xu et al., 2021;Zhai et al., 2020;Wu et al., 2020;Jian et al., 2019;Yu et al., 2019;Mao et al., 2021). The blue points
(3329 valid measurements) represent the observations from Global Surface Seawater DMS Database
(<http://saga.pmel.noaa.gov/dms/>; last access: 1 May 2021). In total, 12 environmental parameters (Table S1) which strongly
affect the growth of phytoplankton and the production of DMS (Wang et al., 2015) were included as predictors in machine
160 learning estimates. Satellite remotely sensed Chlorophyll (Chl), Photosynthetically available Radiation (PAR), Particulate
inorganic/organic Carbon (PIC/POC), and Diffuse attenuation coefficient at 490m (kd_{490}) were from MODIS-Aqua products
(daily,8-day, and monthly Level 3-binned 4km resolution data). Nutrient data (Silicate, Phosphate, and Nitrate), Sea surface



temperature (SST), and Dissolved Oxygen (DO) were obtained from World Ocean Atlas 2018 (monthly 0.25° and 1° climatology data). Monthly mixed layer depth (MLD) climatology ($0.5^\circ \times 0.5^\circ$) was obtained from Monthly Isopycnal & Mixed-layer Ocean Climatology (MIMOC). Before the implementation of the algorithm to Asia's oceans, we performed a model validation. Firstly, the environmental parameters were matched with DMS measurements according to sampling geographical coordinates and date. Take remotely sensed Chl data, for example, if the daily binned data failed to match the DMS observed data, we used the 8-day binned data to take the place of daily binned data. After the data matching, we then conducted filtering and quality control which followed methods from Wang et al., (2020), the number of data points in the simulation domain was reduced from 4351 to 3748 observation-based datasets for in-situ DMS and matched with environmental parameters. Table S1 has a description of the environmental parameters, sources, and their filtering thresholds. To verify the prediction performance of XGBoost model, we divided the datasets into two parts: validation datasets and training datasets. Considering that most of the northern part of the simulation domain was land area, we selected the data from 2° latitude bands between 11°S and 30°N as validation datasets (809 points), while the rest of the data was all used as training data (2939 points).

Figure 1 displays the validation results for XGBoost model, which reproduced DMS concentrations with high correlation coefficients (R) of 0.75 and low root-mean-square error (RMSE) of $1.97 \mu\text{mol m}^{-3}$. The validation statistics are comparable to other studies (R=0.73-0.81 and RMSE=1.92 -2.00 $\mu\text{mol m}^{-3}$) that used nonlinear/multilinear models to predict sea-surface DMS concentrations over the global ocean (Galí et al., 2018; Wang et al., 2020). The advantage of utilizing machine learning method is that the ability of capturing nonlinear relationships between DMS and its affecting parameters to estimate DMS concentrations with a plausible underlying basis in spatial-temporal variability. A shortcoming of the traditional geographical interpolation method is that relatively sparse data is typically interpolated to the entire ocean, which has been highlighted by previous studies (Galí et al., 2015; Galí et al., 2018; Wang et al., 2020). In this study, the advantage of the machine learning method is also demonstrated by comparing two different model simulations (see Section 3.2). In the implementation phase of the machining learning algorithm to regional ocean, to ensure the model was representative of present-day (2017) atmospheric conditions, in addition to climatology environmental parameters, the remotely sensed datasets used to predict DMS concentrations are all from MODIS-Aqua products in 2017. Monthly climatologies were interpolated to the 8-day or monthly periods remotely sensed data; then, we trained XGBoost model to obtain grid values that did not have DMS measurements. Finally, estimated DMS concentration were temporally averaged to a seasonal period and spatially binned to $0.5^\circ \times 0.5^\circ$ grid for Asia region (see Section 3.1).



3 Results

3.1 Spatial and temporal patterns of the sea-water DMS

Regional DMS maps for sea surface DMS concentrations predicted by XGBoost in four seasons are displayed in Figure 2, which showed distinct seasonal variations. The highest regional mean DMS concentrations were observed in the MAM, that is 2.52 $\mu\text{mol m}^{-3}$, approximately 1.15, 1.24, and 1.31 times higher than those in Jun-Jul-Aug (JJA), Sep-Oct-Nov (SON), and Dec-Jan-Feb (DJF) (Table S2), respectively. However, according to the previous studies (Lana et al., 2011; Galí et al., 2018; Wang et al., 2020), the highest DMS concentrations usually occurred in JJA, mainly attributed to adequate solar irradiation and warm temperature being favourable for primary production. We assumed that this difference was caused by different statistical region. Previous results were based on global scale estimates, for comparative purposes, we extracted corresponding simulation domain (Figure 2) estimates values from global scale estimates results, and they were listed in Table S2. Across the Asian Seas, all the highest seasonal mean DMS concentrations occurred in MAM, and our estimates agreed well with the estimates of 2.21-2.33 $\mu\text{mol m}^{-3}$ reported in previous studies (Wang et al., 2020; Lana et al., 2011). As shown in Figure S2, zonal mean DMS concentrations between 10°S and 30°N latitude areas of simulation domain were higher in MAM than in JJA, but those between the 30°N and 50°N latitude band were higher in JJA than in MAM. As mentioned in Section 2.3, most of ocean area is concentrated in 10°S and 30°N latitude band of the entire simulation domain (11°S to 55°N, 60–150°E), which leads to the highest regional mean DMS concentrations being observed in MAM. This is most likely due to the seasonal variation of solar irradiation, because most of ocean area (11°S to 30°N) in the simulation domain was influenced more by the solar irradiation in the MAM than in JJA. A similar result can be found in monthly Hovmöller diagrams of DMS climatologies, depicted by Galí et al. (2018). Throughout the four seasons, there were some high concentrations of DMS (higher than 4.3 $\mu\text{mol m}^{-3}$) that appeared in different coastal areas, which is probably relevant to high nutrient and chlorophyll concentrations over the coastal areas. Galí et al. (2015) also found that most of the coastal regions have higher DMS_{Pt} concentrations compared to the global ocean, and DMS in the sea water was generated from the breakdown of DMS_{Pt}.

We calculated regional sea-air DMS fluxes using the N₀₀ gas transfer velocity and DMS concentrations predicted by XGBoost (Figure 3a). We estimated annual DMS emission fluxes of 1.25 Tg (S), which is 15.4% of the anthropogenic sulfur emissions over the entire simulation domain (covers most of Asia) in 2017. The higher estimated values of DMS fluxes (higher than 250 tonnes (S)/grid) occurred over some coastal waters, which generally agreed well with the estimated sea surface DMS concentration distribution. The highest emission fluxes occurred over the Chinese Seas (reach up to 450 tonnes (S)/grid). These high fluxes can be attributed to local DMS observations dataset in Chinese seas (red point in Figure S1) that were included in the machine learning estimates. Our previous studies (Li et al., 2020a; Li et al., 2020b) have reported that DMS emissions fluxes calculated with the local dataset is 3 times higher than default global-database (Lana et al., 2011) over most area of Chinese Sea. The highest positive changes of DMS emissions fluxes were mainly in the areas of East China Sea (up to 200 tonnes (S)/grid), and some coastal regions (Figure 3b). However, there are more negative changes of DMS emissions fluxes



than positive changes in the sea water, which suggested that sea-air DMS flux estimated in this study generally lower than
225 those from Lana et al. (2011), and the similar result can be found in Wang et al. (2020).

3.2 Model evaluation

3.2.1 Model performance of DMS and its oxidation product MSA

Modelled atmospheric DMS concentrations were compared to observations from 2017 Cruise Survey Experiment (CSE)
1-3 (Figure 4). Due to the discontinuities in time and gaps in observations, we averaged the whole period of each CSE
230 observation for our comparisons. The results in Table S3 demonstrate moderate improvements in the model performance of
DMS predictions when using updated DMS emissions relative to default DMS emissions, i.e., the difference between the
observations and predictions (observation - prediction) became smaller (from -16.34 to 6.68 pptv for CSE 1, -21.11 to -16.17
pptv for CSE 2, and -121.57 to 117.39 pptv for CSE 3, respectively). CSE 3 had much higher DMS concentrations, because
most of the measurements were from the mouth of the Changjiang River, and it is difficult for a coarse model grid ($0.5^\circ \times$
235 0.625°) to represent the high values that occur off coastal areas. MSA is a tracer of DMS, because it is formed exclusively
from DMS (Gondwe et al., 2003). We also evaluated the model performances for MSA by comparing the model simulations
with long-term online measurement site data (Zhou et al., 2021) from Hua Niao Island (Figure 4). Figure 5 displays time series
of daily mean MSA values of predictions (XG and LANA) and observations. The simulated MSA concentrations from XG
and LANA are both within the range of observed values, and the trends of the MSA concentrations were relatively well
240 reproduced, with mean values of 0.014, 0.020, and $0.023 \mu\text{g m}^{-3}$ for LANA, XG, and observations. During the period of Jun
21 to Jun 25 and Jun 28 to July 3, LANA simulation results were closer to the observations, and XG simulations underpredicted
the measurements in those two periods. Overall, the simulation results of XG in other periods were closer to the observations
than those of LANA simulation results.

3.2.2 Model performance evaluation for $\text{PM}_{2.5}$, AOD, and CCN

245 The magnitude and distributions of $\text{PM}_{2.5}$, AOD, and CCN directly influence DRF and IRF estimates. To evaluate whether
GC-TOMAS can reproduce the spatial distribution and temporal trends of these parameters over simulation area, we evaluated
model performance by comparing simulation results for XG with ground observations and satellite-retrieved estimates. Since
the impacts of DMS to $\text{PM}_{2.5}$ and CCN are over the ocean and some coastal areas (see Section 3.3), and the ground
observational data is all over land areas, so we only used one of the simulation results for model evaluation.

250 Boylan and Russell (2006) suggested that when the model performance within the range (mean fractional bias(MFB) \leq
 $\pm 30\%$ and mean fractional error (MFE) $\leq \pm 50\%$), model predictions can be regarded as sufficiently accurate. Figure S3 presents
the distributions of simulated annual mean $\text{PM}_{2.5}$ concentrations and observations at 366 city sites from China National
Environmental Monitoring Center (CNEMC). The model performed well against $\text{PM}_{2.5}$ observations for the year 2017, with
MFB of 5.5% and MFE of 23.1%, both within the goal range, and had a Pearson's correlation coefficient (R) of 0.62. Simulated



255 $PM_{2.5}$ concentrations were slightly underpredicted with a MB of $-1.3 \mu\text{g m}^{-3}$, which is probably ascribed to underpredicted
260 $PM_{2.5}$ in some northern China. Uncertainties in land-based emission inventories tend to cause different model performance in
different regions.

Table S4 summarizes the collected in-situ measurements of CCN concentrations in other previous studies and
corresponding annual-mean simulated CCN concentrations which used for evaluation. The MFB and MFE are 28.17% and
260 34.16%, which meet the suggested benchmark, but the underpredictions of the model estimates are still observed in most areas.
Liu et al., (2020) adopted a satellite-based method to retrieve CCN concentrations from 2013 to 2019, which reported that they
can reasonably reproduce the spatial pattern of CCN in East Asia. In this study, monthly mean GC-TOMAS CCN
concentrations were compared to satellite-retrieved CCN concentrations at supersaturation of approximately 0.2% from Liu et
al., (2020). A total of 8 months of satellite-retrieved CCN concentrations were averaged on MERRA-2 grid (corresponding
265 667 simulation grids) for comparison (Figure S4). The simulated CCN concentrations presented generally similar monthly
variations as the satellite-retrieved concentrations, with MFB of 17.23% and MFE of 37.28%, both meet the criteria suggested
by Boylan and Russell (2006). GC-TOMAS outputted CCN concentrations (430 cm^{-3}) for 8 months were underestimated
compared with satellite-retrieved concentrations (587 cm^{-3}), and this underestimation is more apparent in July, August,
September, and November. However, for other months (February, April, May, and June) the simulated CCN concentrations
270 slightly underpredicted observations with mean bias (MB) of -75 cm^{-3} . This difference is more likely attributable to differences
in model performance in different regions. For example, the underpredictions of CCN in May were mainly distributed in
eastern coastal area of China, the Korean Peninsula, and Japan. But in August and September, the underprediction of model
estimates discrepancies were mainly in the southern and northern part of China, respectively. Due to the limited monitoring
data of CCN in our domain during simulation period, we compared predicted results with satellite-retrieved CCN. However,
275 as Liu et al., (2020) indicated that errors in retrieved data and the CCN counters might cause inaccuracy of satellite CCN
inversion results, it was noted that the satellite derived CCN that cannot be treated as true as in-situ observations during
validating our model results.

For AOD, monthly averages from the Aerosol Robotic Network (AERONET) Version 3 spectral deconvolution algorithm
(SDA) level 2.0 measurements (Giles et al., 2019) were used to validate the model estimations. In total, there are 79
280 measurements within the simulation domain. Figure S5 displays annual-mean model estimates and AERONET measurements
AOD at 550nm (the AERONET AODs at 500nm are converted to 550nm using Ångström exponents at 500nm). The model
estimates compared well with measurements with a Pearson's R of 0.84 and only a slightly underprediction of AOD with MBs
of -0.12. The respective MFB and MFE were -28.64% and 13.45%, which all meet the benchmark suggested in Boylan and
Russel et al, 2006.

285



3.3 Seasonal variations of DMS impacts to SO_4^{2-} , CCN, and radiative forcing

By adding of updated DMS emissions (XG-ND), we predicted the enhancement of near-surface SO_4^{2-} concentrations of 0.1-0.3 $\mu\text{g m}^{-3}$ over most areas of seawater (Figure 6(a)). The highest impacts (approximately 0.3 $\mu\text{g m}^{-3}$) occurred in MAM around the South China Sea area due to highest regional mean DMS concentrations in MAM. However, the spatial distributions of SO_4^{2-} concentrations enhanced by addition of DMS emissions in the four seasons did not exactly follow the spatial and temporal pattern of seawater DMS concentrations (Figure 2). Sea surface wind speed has noticeable impacts on the sea-air DMS flux and followed atmospheric DMS concentrations, which caused higher atmospheric DMS concentrations over the India Ocean in the MAM. Ambient oxidant level also plays an important role in the subsequent DMS oxidation phase. For example, higher atmospheric DMS (300-400pptv) and SO_2 (0.2-0.3 $\mu\text{g m}^{-3}$) concentrations contributed by DMS can be found around the areas of East China Sea (Figure S6 and S7) in MAM and JJA. However, a higher contribution of DMS emissions to near-surface SO_4^{2-} concentrations occurred over south China Sea in DJF and MAM. The spatial disparities might be due to the roles of oxidants in the conversion of SO_2 into SO_4^{2-} in different seasons, and cloud cover could also affect the aqueous conversion.

The magnitude of the all-sky sulfate DRF at TOA contributed by DMS ranged from -200 to -20 mW m^{-2} in four seasons (Figure 6(b)). The spatial patterns of DRF are highly consistent with those of SO_4^{2-} concentrations, with the stronger negative DRF (-200 to -120 mW m^{-2}) in the areas with higher SO_4^{2-} concentrations contributed by DMS, such as the South China Sea, Philippine Sea, and Japan Sea. It should be noted that DRF calculation is from the whole column of the atmosphere whereas Figure 6(a) just shown the surface layer concentrations, yet the spatial results are still qualitatively similar. As reported by some previous studies (Khan et al., 2016; Chen et al., 2018; Zhao et al., 2021), DMS mainly exists in the lower atmosphere, and impacts of DMS to the SO_2 and SO_4^{2-} concentrations are limited to the lower troposphere. So, the magnitude of sulfate DRF at TOA shown in Figure 6(b) is mostly caused by lower-altitude SO_4^{2-} from DMS. SO_4^{2-} aerosols are non-absorbing aerosols primarily scatter incoming radiation, and the increase in reflected solar radiation flux at TOA and almost equally reduce the radiation at the surface (Ramanathan et al., 2001). Thus, for sulfate aerosol, the magnitude of the cooling effect can be estimated from the aerosol radiative forcing at the TOA. The seasonal mean sulfate DRF has a contribution of -22.24, -18.79, -21.58, and -17.43 mW m^{-2} from DMS over the simulation domain in DJF, MAM, JJA, and SON, respectively. The magnitude of the DMS-induced sulfate DRF in DJF and JJA is higher than other seasons, but the highest impacts of DMS emissions on SO_4^{2-} concentrations occurred in MAM followed by DJF. The all-sky DRF was calculated based on the RRTMG model using aerosol mass concentrations (whole column) and optical parameters along with surface albedo and cloud fractions from MERRA-2 assimilated meteorological data. Hence, aerosol mass concentrations as well as other parameters can impact the magnitude and spatial distributions of the DRF. For clear sky condition, aerosol scatter more of incoming solar radiation than in all sky condition, which lead to aerosol DRF at TOA and surface increases compared to all sky conditions.

Figure 7(a) shows the changes in seasonal mean CCN surface concentrations at 0.2% supersaturation (CCN (0.2%)) between the XG - ND simulations. Updated DMS emissions lead to an increase in CCN concentrations by 3 - 42 cm^{-3} over most areas of seawater, and 6 - 16 cm^{-3} in some coastal regions. The highest increases occurred in DJF, followed by MAM.



The impacts of DMS on CCN concentrations are shown in Figure 6(a). The modeled DMS-induced cloud-albedo IRF ranged from -900 to -100 mW m⁻² in four seasons (Figure 7(b)), which is much higher relative to that of the sulfate DRF attributable to DMS. The seasonal mean sulfate IRF had a contribution of -43.29, -45.04, -43.60, and -33.03 mW m⁻² from DMS in our domain in DJF, MAM, JJA, and SON, respectively. There are some similarities in the spatial distributions of the effects of DMS on IRF and CCN. However, the strong negative IRF was mainly over remote oceans (-900 to -600 mW m⁻²), while as for CCN, the higher contributions were concentrated within coastal waters. One explanation for these differences was that strong anthropogenic emissions in Asia led to an intense competition for water vapor during cloud-droplet activation, which further decreased the maximum supersaturation achieved in updrafts and limits droplet activation (Kodros et al., 2016). Also, the clouds are not necessarily at the heights where CCN changes were affected by DMS.

3.4 Annual DMS impacts to SO₄²⁻, CCN, and radiative forcing

3.4.1 Annual DMS impacts to SO₄²⁻, CCN, and radiative forcing between XG and ND simulation

Figure 8 (a) shows the annual-mean percent changes and absolute changes in SO₄²⁻ and CCN between XG and ND simulation. Oceanic DMS emissions increased the near-surface SO₄²⁻ and CCN concentrations by 0.1-0.3 μg m⁻³ and 3 - 42 cm⁻³ over most areas of seawater across the four seasons. Due to heavy amounts of anthropogenic pollutants from the continent, the relative contributions of DMS to SO₄²⁻ and CCN were higher in remote oceanic areas, which reached up to 88% and 42% of all sources. More than 40% and 20% of the SO₄²⁻ and CCN contributed by DMS emissions were also found in the Philippine Sea and India Ocean, respectively. The impact of DMS emissions can cover the entire coastal regions of simulation domain, where DMS had a moderate impact of 0.1-0.18 μg m⁻³ for SO₄²⁻ and 10 -22 cm⁻³ for CCN. Yang et al. (2017) indicated that DMS emissions only have 20-40% of contributions to SO₄²⁻ concentrations over downwind ocean areas of East Asia, which was much lower than 40-70% contributions estimated in this study. This discrepancy is mainly ascribed to a significant reduction (62%) in SO₂ emissions in China from 2010 to 2017 (Zheng et al., 2018).

The modeled all sky DRF of DMS induced sulfate here range from -100 to -10 mW m⁻² (Figure 8 (b)). The sulfate DRF was the strongest (-100 to -60 mW m⁻²) over the South China Sea, which is consistent with the distributions of SO₄²⁻ concentrations contributed by DMS emissions. The DMS induced cloud-albedo IRF (-700 to -100 mW m⁻²) here was higher than the all sky DRF estimate. A relatively strong cooling IRF (-700 to -400 mW m⁻²) induced by DMS emissions can be seen in the vicinity of equatorial belt in India Ocean and northwest Pacific Ocean. The simulated annual mean sulfate DRF and IRF is -20.01 and -41.26 mW m⁻² over the simulation domain, respectively. Li et al. (2019) estimated the annual mean all sky DRF of -100 mW m⁻² from DMS emissions over the East China Sea. Our estimates (-20.01 mW m⁻²) were lower than their result, which is likely attributable to discrepancies in the DMS emissions used to drive the model.



350 3.4.2 Annual DMS impacts to SO_4^{2-} , CCN, and radiative forcing between XG and LANA simulation

To quantify the impacts of DMS emissions changes on SO_4^{2-} , CCN, and radiative forcing, we compared the XG and LANA simulations (Figure S8(a)). Positive impacts for SO_4^{2-} and CCN can be found in the areas of Indonesia and northwest Pacific Ocean (Figure S8(a)), which was generally consistent with the distribution of changes in DMS emissions flux from XG-LANA (Figure 3b). DMS emissions changes (between XG and LANA) accounted for 4-20% and 6-18% of SO_4^{2-} and CCN concentrations over areas of Indonesia, and 2-10% and 3-6% of those concentrations over the northwest Pacific Ocean, respectively. The largest decreases were seen in the vicinity of the India Ocean, which was $-0.06 \mu\text{g m}^{-3}$ for SO_4^{2-} and -10 cm^{-3} for CCN. Due to the higher background concentrations contributed by anthropogenic sources, the relative percent change was smaller over that area, where DMS emissions changes only accounted for -8 to -4 % for SO_4^{2-} and -6 to -3 % for CCN. Also, changes of DMS fluxes around the equatorial belt in western Pacific Ocean (Figure 3b) did not directly link to negative changes in SO_4^{2-} and CCN, which was most likely offset by large scale transport of sulfate caused by DMS from East China Sea. The changes in annual mean DRF and IRF from XG-LANA simulation as shown in Figure S8(b). Negative changes of DRF (-20 to -5 mW m^{-2}) mainly were concentrated over the northwest Pacific Ocean. The largest increase in DRF (up to 40 mW m^{-2}) was found in the areas of the Japan Sea, and most of the positive changes of DRF (5 to 20 mW m^{-2}) were mainly distributed in the region of the Indian Ocean and land areas of India. Their spatial patterns were consistent with distributions of absolute changes of SO_4^{2-} concentrations. The largest changes in IRF were found in areas of the northwest Pacific Ocean and the Sea of Okhotsk, with changes up to -200 and 200 mW m^{-2} . The negative changes of IRF from the XG-LANA simulation can span most Pacific Ocean over the simulation domain and some continental regions, and positive changes of IRF are more concentrated within the India Ocean and Sea of Okhotsk. Generally, our estimated sea-air DMS fluxes are lower than those from Lana et al. (2011) over the most of the ocean areas, but the DMS-caused changes to SO_4^{2-} , CCN, and radiative forcing were more varied, with the positive changes over the northwest Pacific Ocean for SO_4^{2-} and CCN, and negative changes in the regions of India Ocean, oppositely, positive changes in the regions of India Ocean for DRF and IRF, and negative changes over the northwest Pacific Ocean.

3.5 Limitations of this study

We found several limitations in our emission estimates and modeling study. We try to use machine learning estimates of DMS concentrations to fill the regions without observations. However, the primary weakness of the machine learning method is that the training process is not interpretable and not transparent (Reichstein et al., 2019; Wang et al., 2020). The relationship between training parameters should have a minimal physical interpretation, which should be done in future work to give not only accurate but also credible predictions. While the recently measured 1022 seawater DMS observation data over Chinese Seas were included training period, for some months (January, November, etc.), there were still not enough data to create a monthly mean. Hence, we temporally averaged input parameters to a seasonal period rather than use monthly data, which is a



limitation of this study, but as shown in Section 3.1, the estimated results showed distinct seasonal variations, and the results are comparable with other studies. Due to the limited continuous measurements of atmospheric DMS and MSA concentrations, we only presented the averaged each cruise survey observations for DMS model evaluation and temporal variation of MSA prediction performance evaluated only from a single observation site. We acknowledged that this is an important limitation of this study, which prevents us from giving comprehensive estimate (in temporal and spatial scale) of the advantage of our updated DMS emissions. More marine and atmospheric observational data are necessary for further model evaluation.

In addition, due to the limited high temporal resolution monitoring data of CCN for the simulation year 2017 in our domain, we verified the model performance of the CCN simulation by comparing the modeled results with the collected mean annual observed concentrations of CCN in other previous studies and satellite-retrieved CCN concentrations. We acknowledge that the CCN model-measurement comparisons listed in Table S4 are not the exact times where CCN simulated, and satellite-retrieved CCN (given the uncertainty in water uptake and size distributions) are not necessarily accurate enough to represent real atmospheric CCN concentrations in 2017.

Modeled AOD may be biased during cloudy conditions when AERONET measurements may not be available due to missing data. Hence, there would be an uncertainty in using monthly averaged measurements and model predictions for comparison.

Different chemical mechanisms of various chemical-transport models and the treatment of aerosol optical properties can also make differences in simulation results. Globally, the annual-mean DRF and IRF contributed by DMS reported by other studies (as listed in Table S5) varied from -0.23 to -0.074 $W\ m^{-2}$ and -6.55 to -0.3 $W\ m^{-2}$, respectively. Aerosol-cloud interactions are a major source of uncertainty in the prediction of climate change, impacting radiative forcing estimates, especially the IRF calculation. Differences in aerosol nucleation schemes, activation parameterizations, and emissions between models can contribute to large discrepancies in their simulation results (Carslaw et al., 2013). However, we did not explore impact of different nucleation schemes on radiative forcing. We recommend that this should be done in the future work to minimize uncertainties in modeling study.

405 **4 Conclusions**

In this study, we utilized the XGBoost machine learning algorithm to estimate sea-water DMS concentrations by training 12 ocean environmental parameters on newly updated DMS measurements. Recently, 1022 seawater DMS measurements over Chinese Sea were included in our training, and we used the machine learning method to fill the gap at times and in locations without observations. The DMS estimates validation results showed that our XGBoost estimates could capture the observed DMS concentrations with a correlation coefficient of 0.75. Zonal mean DMS concentrations between $10^{\circ}S$ and $30^{\circ}N$ latitude areas of simulation domain were higher in MAM than in JJA, and most of ocean area was concentrated in $10^{\circ}S$ and $30^{\circ}N$ latitude band, which led to the highest regional mean DMS concentrations observed in MAM. We estimated annual DMS emission fluxes of 1.25 Tg (S), which accounted for 15.4% of anthropogenic sulfur emissions over the entire simulation domain (covers most of Asia) in 2017. Comparative analysis revealed that the sea-air DMS flux estimated in this study (from XG



415 estimates) was generally lower than those from global-database DMS emissions (Lana et al., 2011). The model estimates of
DMS and MSA from XG simulation, were evaluated by comparing with cruise survey experiments and long-term online
measurement site data. In general, the improvement in model performance can be observed by comparing with LANA
simulation which uses the global-database DMS emissions.

420 The modeled DMS--induced sulfate DRF and IRF ranged from -200 to -20 mW m⁻² and -900 to -100 mW m⁻² across the
four seasons, respectively. The stronger negative DRF (-120 to -200 mW m⁻²) were in the areas where with higher SO₄²⁻
concentrations contributed by DMS, such as the South China Sea, Philippine Sea, and Japan Sea. However, the strong negative
IRF was mainly over remote oceans (-900 to -600 mW m⁻²), which did not match with the spatial distributions of contributions
of DMS to CCN concentrations due to the role of clouds in the IRF. Annually, DMS--induced sulfate IRF (-700 to -100 mW
m⁻²) here obviously higher than those all sky DRF (-100 to -10 mW m⁻²). By adding our updated DMS emissions to a simulation
425 with no DMS (XG-ND), we predict the enhancement of near-surface SO₄²⁻ and CCN concentrations by 0.1-0.3 μg m⁻³ and 3 -
42 cm⁻³, respectively, over most oceanic areas in all four seasons. We found higher contributions from DMS emissions to SO₄²⁻
and CCN in MAM and DJF than JJA and SON.

430 In this work, we quantified the contributions of DMS to atmospheric SO₄²⁻ and CCN aerosol concentrations along with
their radiative effect over a modeled Asian domain (covers most of Asia). This work provides better insights into the source
strength of DMS and its impact on climate, addressing knowledge gaps related to factors controlling aerosols in the marine
boundary layer and their climate impacts. As discussed in Section 3.6, there are several limitations that need to be improved
in the future work. More marine and atmospheric observational data are necessary for further DMS emission estimates and
model evaluation to explore the interactions of DMS with aerosols and radiative forcing. In the future work, we also need to
435 explore the impact of different aerosol nucleation schemes on radiative forcing, to more completely quantify the uncertainties
our modeling study.

440

Competing interests. The authors declare that they have no conflict of interest.

445

Acknowledgements. This work was supported by the National Key Research and Development Program of China (Grant
2016YFA060130X), the Major Program of Shanghai Committee of Science and Technology, China (19DZ1205009), and the
National Natural Science Foundation of China (42077195).



References

- 450 Abdul-Razzak, H., and Ghan, S. J.: A parameterization of aerosol activation 3. Sectional representation, *Journal of Geophysical Research: Atmospheres*, 107, AAC 1-1-AAC 1-6, <https://doi.org/10.1029/2001JD000483>, 2002.
- Adams, P. J., and Seinfeld, J. H.: Predicting global aerosol size distributions in general circulation models, *Journal of Geophysical Research: Atmospheres*, 107, AAC 4-1-AAC 4-23, <https://doi.org/10.1029/2001JD001010>, 2002.
- 455 Alexander, B., Park, R. J., Jacob, D. J., Li, Q. B., Yantosca, R. M., Savarino, J., Lee, C. C. W., and Thiemens, M. H.: Sulfate formation in sea-salt aerosols: Constraints from oxygen isotopes, *Journal of Geophysical Research: Atmospheres*, 110, <https://doi.org/10.1029/2004JD005659>, 2005.
- Amos, H. M., Jacob, D. J., Holmes, C. D., Fisher, J. A., Wang, Q., Yantosca, R. M., Corbitt, E. S., Galarneau, E., Rutter, A. P., Gustin, M. S., Steffen, A., Schauer, J. J., Graydon, J. A., Louis, V. L. S., Talbot, R. W., Edgerton, E. S., Zhang, Y., and Sunderland, E. M.: Gas-particle partitioning of atmospheric Hg(II) and its effect on global mercury deposition, *Atmos. Chem. Phys.*, 12, 591-603, 10.5194/acp-12-591-2012, 460 2012.
- Andreae, M. O., and Rosenfeld, D.: Aerosol–cloud–precipitation interactions. Part 1. The nature and sources of cloud-active aerosols, *Earth-Science Reviews*, 89, 13-41, <https://doi.org/10.1016/j.earscirev.2008.03.001>, 2008.
- Bell, T. G., Porter, J. G., Wang, W.-L., Lawler, M. J., Boss, E., Behrenfeld, M. J., and Saltzman, E. S.: Predictability of Seawater DMS During the North Atlantic Aerosol and Marine Ecosystem Study (NAAMES), 7, 10.3389/fmars.2020.596763, 2021.
- 465 Bey, I., Jacob, D. J., Yantosca, R. M., Logan, J. A., Field, B. D., Fiore, A. M., Li, Q., Liu, H. Y., Mickley, L. J., and Schultz, M. G.: Global modeling of tropospheric chemistry with assimilated meteorology: Model description and evaluation, *Journal of Geophysical Research: Atmospheres*, 106, 23073-23095, <https://doi.org/10.1029/2001JD000807>, 2001.
- Bilsback, K. R., Baumgartner, J., Cheeseman, M., Ford, B., Kodros, J. K., Li, X., Ramnarine, E., Tao, S., Zhang, Y., Carter, E., and Pierce, J. R.: Estimated Aerosol Health and Radiative Effects of the Residential Coal Ban in the Beijing-Tianjin-Hebei Region of China, *Aerosol and Air Quality Research*, 20, 2332-2346, 10.4209/aaqr.2019.11.0565, 2020a.
- 470 Bilsback, K. R., Kerry, D., Croft, B., Ford, B., Jathar, S. H., Carter, E., Martin, R. V., and Pierce, J. R.: Beyond SO_x reductions from shipping: assessing the impact of NO_x and carbonaceous-particle controls on human health and climate, *Environmental Research Letters*, 15, 124046, 10.1088/1748-9326/abc718, 2020b.
- Bohren, C. F., and Huffman, D. R.: Absorption and scattering of light by small particles, 1983.
- 475 Boylan, J. W., and Russell, A. G.: PM and light extinction model performance metrics, goals, and criteria for three-dimensional air quality models, *Atmospheric Environment*, 40, 4946-4959, <https://doi.org/10.1016/j.atmosenv.2005.09.087>, 2006.
- Carslaw, K. S., Lee, L. A., Reddington, C. L., Pringle, K. J., Rap, A., Forster, P. M., Mann, G. W., Spracklen, D. V., Woodhouse, M. T., Regayre, L. A., and Pierce, J. R.: Large contribution of natural aerosols to uncertainty in indirect forcing, *Nature*, 503, 67-71, 10.1038/nature12674, 2013.
- 480 Charlson, R. J., Lovelock, J. E., Andreae, M. O., and Warren, S. G.: Oceanic phytoplankton, atmospheric sulphur, cloud albedo and climate, *Nature*, 326, 655-661, 10.1038/326655a0, 1987.
- Chen, Q., Sherwen, T., Evans, M., and Alexander, B.: DMS oxidation and sulfur aerosol formation in the marine troposphere: a focus on reactive halogen and multiphase chemistry, *Atmos. Chem. Phys.*, 18, 13617-13637, 10.5194/acp-18-13617-2018, 2018.
- Chen, T., and Guestrin, C.: XGBoost: A Scalable Tree Boosting System, *Proceedings of the 22nd ACM SIGKDD International Conference on Knowledge Discovery and Data Mining*, San Francisco, California, USA, 2016.
- 485 Choi, Y.-N., Song, S.-K., Lee, S. H., and Moon, J.-H.: Estimation of marine dimethyl sulfide emissions from East Asian seas and their impact on natural direct radiative forcing, *Atmospheric Environment*, 222, 117165, <https://doi.org/10.1016/j.atmosenv.2019.117165>, 2020.
- D'Andrea, S. D., Häkkinen, S. A. K., Westervelt, D. M., Kuang, C., Levin, E. J. T., Kanawade, V. P., Leaich, W. R., Spracklen, D. V., Riipinen, I., and Pierce, J. R.: Understanding global secondary organic aerosol amount and size-resolved condensational behavior, *Atmos. Chem. Phys.*, 13, 11519-11534, 10.5194/acp-13-11519-2013, 2013.
- 490 Duncan Fairlie, T., Jacob, D. J., and Park, R. J.: The impact of transpacific transport of mineral dust in the United States, *Atmospheric Environment*, 41, 1251-1266, <https://doi.org/10.1016/j.atmosenv.2006.09.048>, 2007.
- Fountoukis, C., and Nenes, A.: ISORROPIA II: a computationally efficient thermodynamic equilibrium model for K^{+} – Ca^{2+} – Mg^{2+} – NH_4^{+} – Na^{+} – SO_4^{2-} – NO_3^{-} – Cl^{-} – H_2O aerosols, *Atmos. Chem. Phys.*, 7, 4639-4659, 10.5194/acp-7-4639-2007, 2007.
- Galí, M., Devred, E., Levasseur, M., Royer, S.-J., and Babin, M.: A remote sensing algorithm for planktonic dimethylsulfoniopropionate (DMSP) and an analysis of global patterns, *Remote Sensing of Environment*, 171, 171-184, <https://doi.org/10.1016/j.rse.2015.10.012>, 2015.
- Galí, M., Levasseur, M., Devred, E., Simó, R., and Babin, M.: Sea-surface dimethylsulfide (DMS) concentration from satellite data at global and regional scales, *Biogeosciences*, 15, 3497-3519, 10.5194/bg-15-3497-2018, 2018.
- 500 Gelaro, R., McCarty, W., Suárez, M. J., Todling, R., Molod, A., Takacs, L., Randles, C. A., Darmenov, A., Bosilovich, M. G., Reichle, R., Wargan, K., Coy, L., Cullather, R., Draper, C., Akella, S., Buchard, V., Conaty, A., da Silva, A. M., Gu, W., Kim, G.-K., Koster, R., Lucchesi, R., Merkova, D., Nielsen, J. E., Partyka, G., Pawson, S., Putman, W., Rienecker, M., Schubert, S. D., Sienkiewicz, M., and Zhao, B.: The



- 505 Modern-Era Retrospective Analysis for Research and Applications, Version 2 (MERRA-2), *Journal of Climate*, 30, 5419-5454, 10.1175/JCLI-D-16-0758.1, 2017.
- Giles, D. M., Sinyuk, A., Sorokin, M. G., Schafer, J. S., Smirnov, A., Slutsker, I., Eck, T. F., Holben, B. N., Lewis, J. R., Campbell, J. R., Welton, E. J., Korkin, S. V., and Lyapustin, A. I.: Advancements in the Aerosol Robotic Network (AERONET) Version 3 database – automated near-real-time quality control algorithm with improved cloud screening for Sun photometer aerosol optical depth (AOD) measurements, *Atmos. Meas. Tech.*, 12, 169-209, 10.5194/amt-12-169-2019, 2019.
- 510 Gondwe, M., Krol, M., Gieskes, W., Klaassen, W., and de Baar, H.: The contribution of ocean-leaving DMS to the global atmospheric burdens of DMS, MSA, SO₂, and NSS SO₄, *Global Biogeochemical Cycles*, 17, 10.1029/2002GB001937, 2003.
- Guenther, A. B., Jiang, X., Heald, C. L., Sakulyanontvittaya, T., Duhl, T., Emmons, L. K., and Wang, X.: The Model of Emissions of Gases and Aerosols from Nature version 2.1 (MEGAN2.1): an extended and updated framework for modeling biogenic emissions, *Geosci. Model Dev.*, 5, 1471-1492, 10.5194/gmd-5-1471-2012, 2012.
- 515 Hodshire, A. L., Campuzano-Jost, P., Kodros, J. K., Croft, B., Nault, B. A., Schroder, J. C., Jimenez, J. L., and Pierce, J. R.: The potential role of methanesulfonic acid (MSA) in aerosol formation and growth and the associated radiative forcings, *Atmos. Chem. Phys.*, 19, 3137-3160, 10.5194/acp-19-3137-2019, 2019.
- Hudman, R. C., Moore, N. E., Mebust, A. K., Martin, R. V., Russell, A. R., Valin, L. C., and Cohen, R. C.: Steps towards a mechanistic model of global soil nitric oxide emissions: implementation and space based-constraints, *Atmos. Chem. Phys.*, 12, 7779-7795, 10.5194/acp-12-7779-2012, 2012.
- 520 Iacono, M. J., Delamere, J. S., Mlawer, E. J., Shephard, M. W., Clough, S. A., and Collins, W. D.: Radiative forcing by long-lived greenhouse gases: Calculations with the AER radiative transfer models, *Journal of Geophysical Research: Atmospheres*, 113, <https://doi.org/10.1029/2008JD009944>, 2008.
- Jian, S., Zhang, H.-H., Yang, G.-P., and Li, G.-L.: Variation of biogenic dimethylated sulfur compounds in the Changjiang River Estuary and the coastal East China Sea during spring and summer, *Journal of Marine Systems*, 199, 103222, <https://doi.org/10.1016/j.jmarsys.2019.103222>, 2019.
- 525 Jin, Q., Grandey, B. S., Rothenberg, D., Avramov, A., and Wang, C.: Impacts on cloud radiative effects induced by coexisting aerosols converted from international shipping and maritime DMS emissions, *Atmos. Chem. Phys.*, 18, 16793-16808, 10.5194/acp-18-16793-2018, 2018.
- 530 Kettle, A. J., Andreae, M. O., Amouroux, D., Andreae, T. W., Bates, T. S., Berresheim, H., Bingemer, H., Boniforti, R., Curran, M. A. J., DiTullio, G. R., Helas, G., Jones, G. B., Keller, M. D., Kiene, R. P., Leck, C., Lelasseur, M., Malin, G., Maspero, M., Matrai, P., McTaggart, A. R., Mihalopoulos, N., Nguyen, B. C., Novo, A., Putaud, J. P., Rapsomanikis, S., Roberts, G., Schebeske, G., Sharma, S., Simó, R., Staubes, R., Turner, S., and Uher, G.: A global database of sea surface dimethylsulfide (DMS) measurements and a procedure to predict sea surface DMS as a function of latitude, longitude, and month, *Global Biogeochemical Cycles*, 13, 399-444, 10.1029/1999GB900004, 1999.
- 535 Khan, M. A. H., Gillespie, S. M. P., Razis, B., Xiao, P., Davies-Coleman, M. T., Percival, C. J., Derwent, R. G., Dyke, J. M., Ghosh, M. V., Lee, E. P. F., and Shallcross, D. E.: A modelling study of the atmospheric chemistry of DMS using the global model, STOCHEM-CRI, *Atmospheric Environment*, 127, 69-79, <https://doi.org/10.1016/j.atmosenv.2015.12.028>, 2016.
- Kodros, J. K., Cucinotta, R., Ridley, D. A., Wiedinmyer, C., and Pierce, J. R.: The aerosol radiative effects of uncontrolled combustion of domestic waste, *Atmos. Chem. Phys.*, 16, 6771-6784, 10.5194/acp-16-6771-2016, 2016.
- 540 Kodros, J. K., and Pierce, J. R.: Important global and regional differences in aerosol cloud-albedo effect estimates between simulations with and without prognostic aerosol microphysics, *Journal of Geophysical Research: Atmospheres*, 122, 4003-4018, <https://doi.org/10.1002/2016JD025886>, 2017.
- Koepke, P., Hess, M., Schult, I., and Shettle, E.: Global aerosol data set, in, report, 1997.
- 545 Kulmala, M., Petäjä, T., Ehn, M., Thornton, J., Sipilä, M., Worsnop, D. R., and Kerminen, V. M.: Chemistry of Atmospheric Nucleation: On the Recent Advances on Precursor Characterization and Atmospheric Cluster Composition in Connection with Atmospheric New Particle Formation, *Annual Review of Physical Chemistry*, 65, 21-37, 10.1146/annurev-physchem-040412-110014, 2014.
- Lana, A., Bell, T. G., Simó, R., Vallina, S. M., Ballabrera-Poy, J., Kettle, A. J., Dachs, J., Bopp, L., Saltzman, E. S., Stefels, J., Johnson, J. E., and Liss, P. S.: An updated climatology of surface dimethylsulfide concentrations and emission fluxes in the global ocean, *Global Biogeochemical Cycles*, 25, 10.1029/2010GB003850, 2011.
- 550 Lee, Y. H., Chen, K., and Adams, P. J.: Development of a global model of mineral dust aerosol microphysics, *Atmos. Chem. Phys.*, 9, 2441-2458, 10.5194/acp-9-2441-2009, 2009.
- Lee, Y. H., and Adams, P. J.: A Fast and Efficient Version of the Two-Moment Aerosol Sectional (TOMAS) Global Aerosol Microphysics Model, *Aerosol Science and Technology*, 46, 678-689, 10.1080/02786826.2011.643259, 2012.
- 555 Lee, Y. H., Pierce, J. R., and Adams, P. J.: Representation of nucleation mode microphysics in a global aerosol model with sectional microphysics, *Geosci. Model Dev.*, 6, 1221-1232, 10.5194/gmd-6-1221-2013, 2013.
- Li, J., Han, Z., Yao, X., Xie, Z., and Tan, S.: The distributions and direct radiative effects of marine aerosols over East Asia in springtime, *Science of The Total Environment*, 651, 1913-1925, <https://doi.org/10.1016/j.scitotenv.2018.09.368>, 2019.



- Li, S., Sarwar, G., Zhao, J., Zhang, Y., Zhou, S., Chen, Y., Yang, G., and Saiz-Lopez, A.: Modeling the Impact of Marine DMS Emissions on Summertime Air Quality Over the Coastal East China Seas, *Earth and Space Science*, 7, e2020EA001220, <https://doi.org/10.1029/2020EA001220>, 2020a.
- Li, S., Zhang, Y., Zhao, J., Sarwar, G., Zhou, S., Chen, Y., Yang, G., and Saiz-Lopez, A.: Regional and Urban-Scale Environmental Influences of Oceanic DMS Emissions over Coastal China Seas, *Atmosphere*, 11, 10.3390/atmos11080849, 2020b.
- Liu, C., Wang, T., Rosenfeld, D., Zhu, Y., Yue, Z., Yu, X., Xie, X., Li, S., Zhuang, B., Cheng, T., and Niu, S.: Anthropogenic Effects on Cloud Condensation Nuclei Distribution and Rain Initiation in East Asia, *Geophysical Research Letters*, 47, e2019GL086184, <https://doi.org/10.1029/2019GL086184>, 2020.
- Liu, H., Jacob, D. J., Bey, I., and Yantosca, R. M.: Constraints from ²¹⁰Pb and ⁷Be on wet deposition and transport in a global three-dimensional chemical tracer model driven by assimilated meteorological fields, *Journal of Geophysical Research: Atmospheres*, 106, 12109-12128, <https://doi.org/10.1029/2000JD900839>, 2001.
- Mahajan, A. S., Fadnavis, S., Thomas, M. A., Pozzoli, L., Gupta, S., Royer, S.-J., Saiz-Lopez, A., and Simó, R.: Quantifying the impacts of an updated global dimethyl sulfide climatology on cloud microphysics and aerosol radiative forcing, *Journal of Geophysical Research: Atmospheres*, 120, 2524-2536, <https://doi.org/10.1002/2014JD022687>, 2015.
- Mao, S.-H., Zhuang, G.-C., Liu, X.-W., Jin, N., Zhang, H.-H., Montgomery, A., Liu, X.-T., and Yang, G.-P.: Seasonality of dimethylated sulfur compounds cycling in north China marginal seas, *Marine Pollution Bulletin*, 170, 112635, <https://doi.org/10.1016/j.marpolbul.2021.112635>, 2021.
- McDuffie, E. E., Smith, S. J., O'Rourke, P., Tibrewal, K., Venkataraman, C., Marais, E. A., Zheng, B., Crippa, M., Brauer, M., and Martin, R. V.: A global anthropogenic emission inventory of atmospheric pollutants from sector- and fuel-specific sources (1970–2017): an application of the Community Emissions Data System (CEDS), *Earth Syst. Sci. Data*, 12, 3413-3442, 10.5194/essd-12-3413-2020, 2020.
- Nightingale, P. D., Malin, G., Law, C. S., Watson, A. J., Liss, P. S., Liddicoat, M. I., Boutin, J., and Upstill-Goddard, R. C.: In situ evaluation of air-sea gas exchange parameterizations using novel conservative and volatile tracers, *Global Biogeochemical Cycles*, 14, 373-387, 10.1029/1999GB900091, 2000.
- Park, K. T., Jang, S., Lee, K., Yoon, Y. J., Kim, M. S., Park, K., Cho, H. J., Kang, J. H., Udisti, R., Lee, B. Y., and Shin, K. H.: Observational evidence for the formation of DMS-derived aerosols during Arctic phytoplankton blooms, *Atmos. Chem. Phys.*, 17, 9665-9675, 10.5194/acp-17-9665-2017, 2017.
- Park, R. J., Jacob, D. J., Field, B. D., Yantosca, R. M., and Chin, M.: Natural and transboundary pollution influences on sulfate-nitrate-ammonium aerosols in the United States: Implications for policy, *Journal of Geophysical Research: Atmospheres*, 109, <https://doi.org/10.1029/2003JD004473>, 2004.
- Pierce, J. R., and Adams, P. J.: Global evaluation of CCN formation by direct emission of sea salt and growth of ultrafine sea salt, *Journal of Geophysical Research: Atmospheres*, 111, <https://doi.org/10.1029/2005JD006186>, 2006.
- Pierce, J. R., Chen, K., and Adams, P. J.: Contribution of primary carbonaceous aerosol to cloud condensation nuclei: processes and uncertainties evaluated with a global aerosol microphysics model, *Atmos. Chem. Phys.*, 7, 5447-5466, 10.5194/acp-7-5447-2007, 2007.
- Price, C., and Rind, D.: A simple lightning parameterization for calculating global lightning distributions, *Journal of Geophysical Research: Atmospheres*, 97, 9919-9933, <https://doi.org/10.1029/92JD00719>, 1992.
- Pye, H. O. T., Liao, H., Wu, S., Mickley, L. J., Jacob, D. J., Henze, D. K., and Seinfeld, J. H.: Effect of changes in climate and emissions on future sulfate-nitrate-ammonium aerosol levels in the United States, *Journal of Geophysical Research: Atmospheres*, 114, <https://doi.org/10.1029/2008JD010701>, 2009.
- Quinn, P. K., and Bates, T. S.: The case against climate regulation via oceanic phytoplankton sulphur emissions, *Nature*, 480, 51-56, 10.1038/nature10580, 2011.
- Quinn, P. K., Coffman, D. J., Johnson, J. E., Upchurch, L. M., and Bates, T. S.: Small fraction of marine cloud condensation nuclei made up of sea spray aerosol, *Nature Geoscience*, 10, 674-679, 10.1038/ngeo3003, 2017.
- Ramanathan, V., Crutzen, P. J., Kiehl, J. T., and Rosenfeld, D.: Aerosols, Climate, and the Hydrological Cycle, *Science*, 294, 2119-2124, 10.1126/science.1064034, 2001.
- Rap, A., Scott, C. E., Spracklen, D. V., Bellouin, N., Forster, P. M., Carslaw, K. S., Schmidt, A., and Mann, G.: Natural aerosol direct and indirect radiative effects, *Geophysical Research Letters*, 40, 3297-3301, <https://doi.org/10.1002/grl.50441>, 2013.
- Reichstein, M., Camps-Valls, G., Stevens, B., Jung, M., Denzler, J., Carvalhais, N., and Prabhat: Deep learning and process understanding for data-driven Earth system science, *Nature*, 566, 195-204, 10.1038/s41586-019-0912-1, 2019.
- Scott, C. E., Rap, A., Spracklen, D. V., Forster, P. M., Carslaw, K. S., Mann, G. W., Pringle, K. J., Kivekäs, N., Kulmala, M., Lihavainen, H., and Tunved, P.: The direct and indirect radiative effects of biogenic secondary organic aerosol, *Atmos. Chem. Phys.*, 14, 447-470, 10.5194/acp-14-447-2014, 2014.
- Thomas, M. A., Suntharalingam, P., Pozzoli, L., Rast, S., Devasthale, A., Kloster, S., Feichter, J., and Lenton, T. M.: Quantification of DMS aerosol-cloud-climate interactions using the ECHAM5-HAMMOZ model in a current climate scenario, *Atmos. Chem. Phys.*, 10, 7425-7438, 10.5194/acp-10-7425-2010, 2010.
- Trivitanurak, W., Adams, P. J., Spracklen, D. V., and Carslaw, K. S.: Tropospheric aerosol microphysics simulation with assimilated meteorology: model description and intermodel comparison, *Atmos. Chem. Phys.*, 8, 3149-3168, 10.5194/acp-8-3149-2008, 2008.



- 615 Vallina, S. M., and Simó, R.: Strong Relationship Between DMS and the Solar Radiation Dose over the Global Surface Ocean, *Science*, 315, 506, 10.1126/science.1133680, 2007.
- van der Werf, G. R., Randerson, J. T., Giglio, L., van Leeuwen, T. T., Chen, Y., Rogers, B. M., Mu, M., van Marle, M. J. E., Morton, D. C., Collatz, G. J., Yokelson, R. J., and Kasibhatla, P. S.: Global fire emissions estimates during 1997–2016, *Earth Syst. Sci. Data*, 9, 697–720, 10.5194/essd-9-697-2017, 2017.
- 620 Wang, S., Elliott, S., Maltrud, M., and Cameron-Smith, P.: Influence of explicit Phaeocystis parameterizations on the global distribution of marine dimethyl sulfide, *Journal of Geophysical Research: Biogeosciences*, 120, 2158–2177, <https://doi.org/10.1002/2015JG003017>, 2015.
- Wang, W. L., Song, G., Primeau, F., Saltzman, E. S., Bell, T. G., and Moore, J. K.: Global ocean dimethyl sulfide climatology estimated from observations and an artificial neural network, *Biogeosciences*, 17, 5335–5354, 10.5194/bg-17-5335-2020, 2020.
- Wang, Y., Jacob, D. J., and Logan, J. A.: Global simulation of tropospheric O₃-NO_x-hydrocarbon chemistry: 1. Model formulation, *Journal of Geophysical Research: Atmospheres*, 103, 10713–10725, <https://doi.org/10.1029/98JD00158>, 1998.
- 625 Wesely, M. L.: Parameterization of surface resistances to gaseous dry deposition in regional-scale numerical models, *Atmospheric Environment*, 41, 52–63, <https://doi.org/10.1016/j.atmosenv.2007.10.058>, 2007.
- Westervelt, D. M., Pierce, J. R., Riipinen, I., Trivitayanurak, W., Hamed, A., Kulmala, M., Laaksonen, A., Decesari, S., and Adams, P. J.: Formation and growth of nucleated particles into cloud condensation nuclei: model–measurement comparison, *Atmos. Chem. Phys.*, 13, 7645–7663, 10.5194/acp-13-7645-2013, 2013.
- 630 Wu, X., Li, P. F., Zhang, H. H., Zhu, M. X., Liu, C. Y., and Yang, G. P.: Acrylic acid and related dimethylated sulfur compounds in the Bohai and Yellow seas during summer and winter, *Biogeosciences*, 17, 1991–2008, 10.5194/bg-17-1991-2020, 2020.
- Xu, F., Yan, S.-B., Zhang, H.-H., Wu, Y.-C., Ma, Q.-Y., Song, Y.-C., Zhuang, G.-C., and Yang, G.-P.: Occurrence and cycle of dimethyl sulfide in the western Pacific Ocean, *Limnology and Oceanography*, n/a, <https://doi.org/10.1002/lno.11797>, 2021.
- 635 Yang, G.-P., Song, Y.-Z., Zhang, H.-H., Li, C.-X., and Wu, G.-W.: Seasonal variation and biogeochemical cycling of dimethylsulfide (DMS) and dimethylsulfoniopropionate (DMSP) in the Yellow Sea and Bohai Sea, *Journal of Geophysical Research: Oceans*, 119, 8897–8915, <https://doi.org/10.1002/2014JC010373>, 2014.
- Yang, G.-P., Zhang, S.-H., Zhang, H.-H., Yang, J., and Liu, C.-Y.: Distribution of biogenic sulfur in the Bohai Sea and northern Yellow Sea and its contribution to atmospheric sulfate aerosol in the late fall, *Marine Chemistry*, 169, 23–32, <https://doi.org/10.1016/j.marchem.2014.12.008>, 2015a.
- 640 Yang, J., Yang, G., Zhang, H., and Zhang, S.: Spatial distribution of dimethylsulfide and dimethylsulfoniopropionate in the Yellow Sea and Bohai Sea during summer, *Chinese Journal of Oceanology and Limnology*, 33, 1020–1038, 10.1007/s00343-015-4188-5, 2015b.
- Yang, Y., Wang, H., Smith, S. J., Easter, R., Ma, P. L., Qian, Y., Yu, H., Li, C., and Rasch, P. J.: Global source attribution of sulfate concentration and direct and indirect radiative forcing, *Atmos. Chem. Phys.*, 17, 8903–8922, 10.5194/acp-17-8903-2017, 2017.
- 645 Yu, J., Tian, J. Y., Zhang, Z. Y., Yang, G. P., Chen, H. J., Xu, R., and Chen, R.: Role of *Calanus sinicus* (Copepoda, Calanoida) on Dimethylsulfide and Dimethylsulfoniopropionate Production in Jiaozhou Bay, *Journal of Geophysical Research: Biogeosciences*, 124, 2481–2498, <https://doi.org/10.1029/2018JG004721>, 2019.
- Zender, C. S., Bian, H., and Newman, D.: Mineral Dust Entrainment and Deposition (DEAD) model: Description and 1990s dust climatology, *Journal of Geophysical Research: Atmospheres*, 108, <https://doi.org/10.1029/2002JD002775>, 2003.
- 650 Zhai, X., Song, Y.-C., Li, J.-L., Yang, J., Zhang, H.-H., and Yang, G.-P.: Distribution Characteristics of Dimethylated Sulfur Compounds and Turnover of Dimethylsulfide in the Northern South China Sea During Summer, *Journal of Geophysical Research: Biogeosciences*, 125, e2019JG005363, <https://doi.org/10.1029/2019JG005363>, 2020.
- Zhao, J., Sarwar, G., Gantt, B., Foley, K., Henderson, B. H., Pye, H. O. T., Fahey, K. M., Kang, D., Mathur, R., Zhang, Y., Li, Q., and Saiz-Lopez, A.: Impact of dimethylsulfide chemistry on air quality over the Northern Hemisphere, *Atmospheric Environment*, 244, 117961, <https://doi.org/10.1016/j.atmosenv.2020.117961>, 2021.
- 655 Zheng, B., Tong, D., Li, M., Liu, F., Hong, C., Geng, G., Li, H., Li, X., Peng, L., Qi, J., Yan, L., Zhang, Y., Zhao, H., Zheng, Y., He, K., and Zhang, Q.: Trends in China's anthropogenic emissions since 2010 as the consequence of clean air actions, *Atmos. Chem. Phys.*, 18, 14095–14111, 10.5194/acp-18-14095-2018, 2018.
- Zhou, S., Chen, Y., Paytan, A., Li, H., Wang, F., Zhu, Y., Yang, T., Zhang, Y., and Zhang, R.: Non-Marine Sources Contribute to Aerosol Methanesulfonate Over Coastal Seas, *Journal of Geophysical Research: Atmospheres*, 126, e2021JD034960, <https://doi.org/10.1029/2021JD034960>, 2021.
- 660

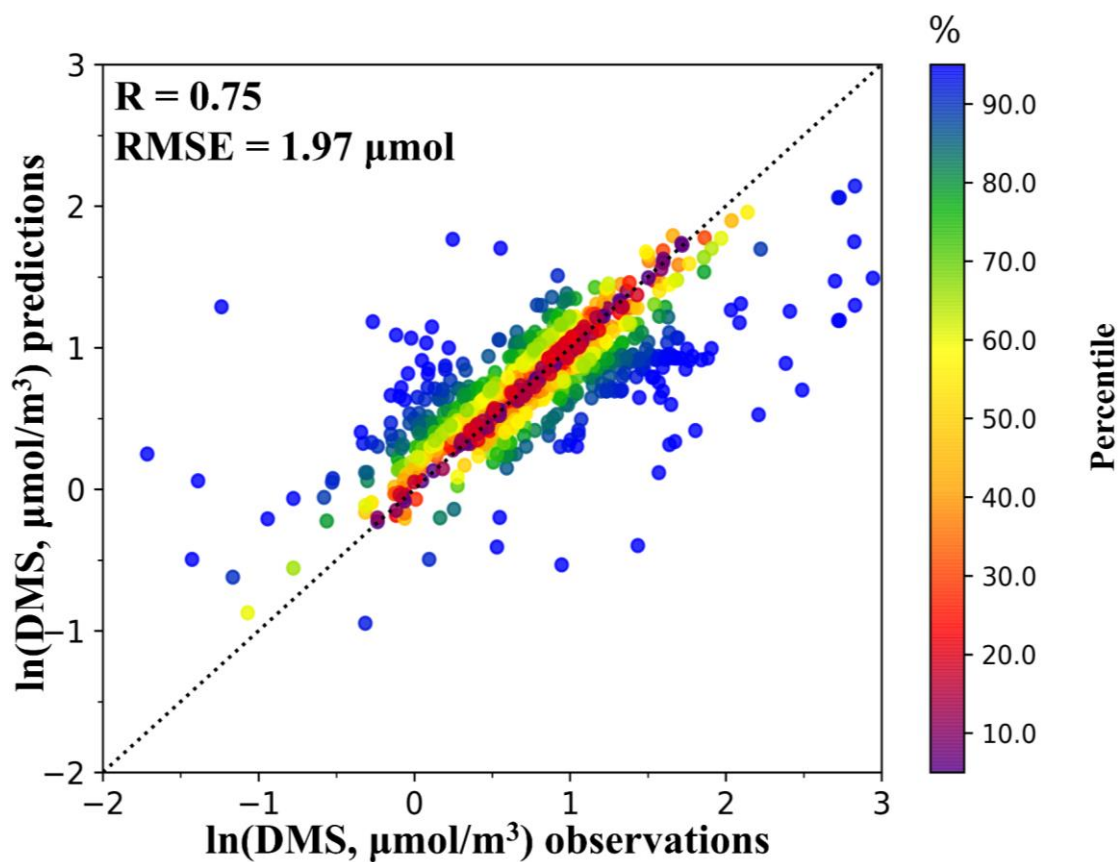


Figure 1. The scatter plot compares model predictions and observations of DMS. The colour represents the percentile of distribution of absolute difference between predicted and observation data.

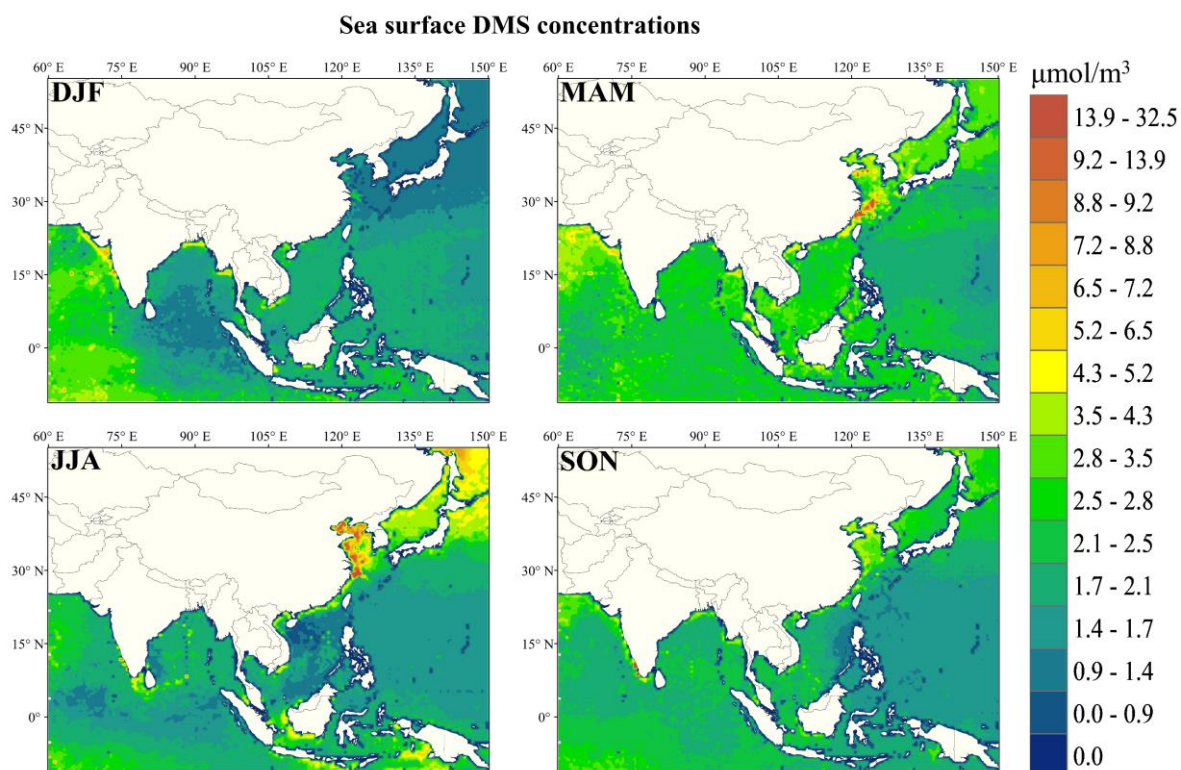
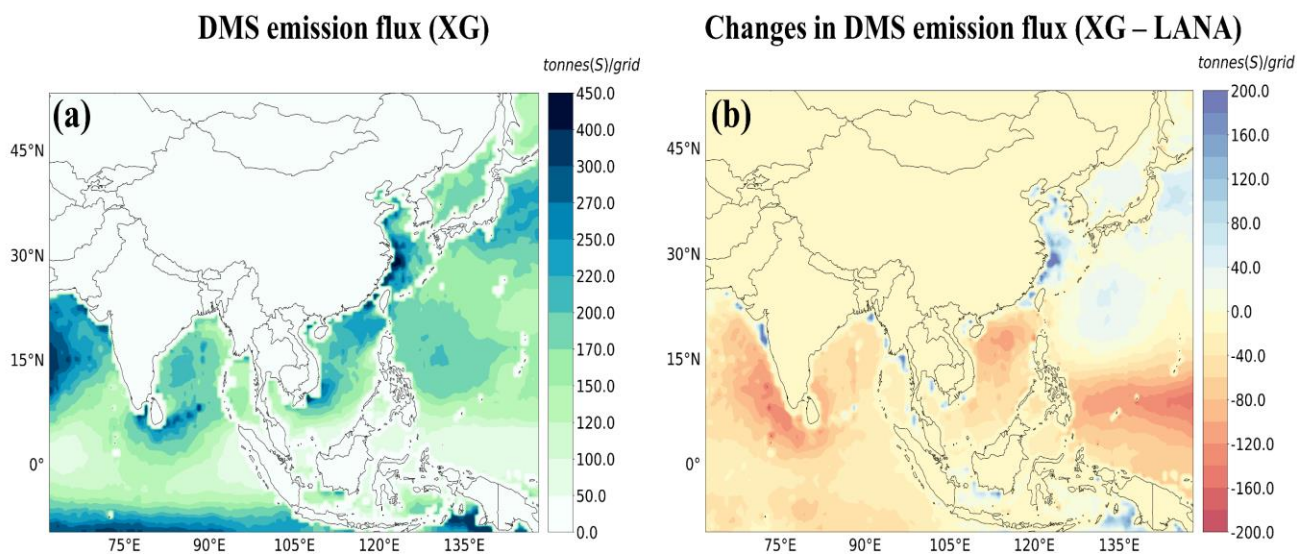
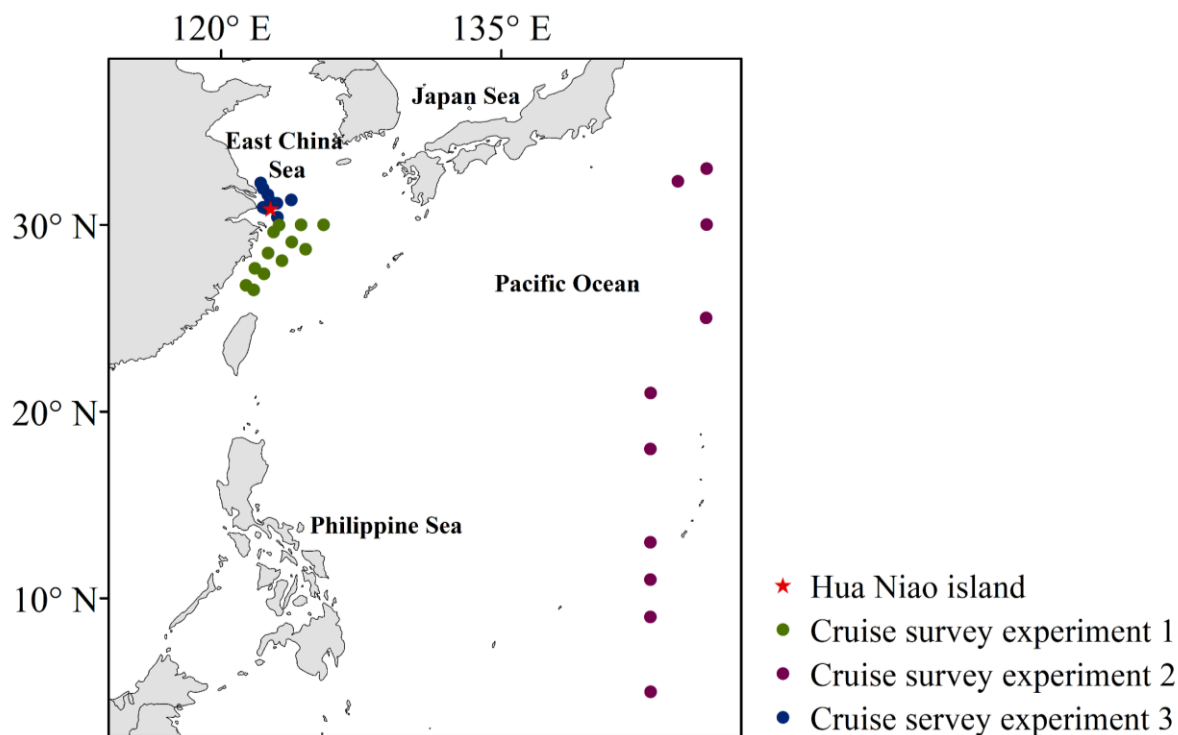


Figure 2. Sea-surface DMS concentrations predicted by XGBoost model by season.



670 **Figure 3.** Panel (a) presents Annual DMS emission flux calculated based on N00 flux parameterization (Nightingale et al., 2000) from XG sea surface concentrations, panel (b) presents changes between DMS emission flux from updated (XG) and default climatology (LANA).



675 **Figure 4.** Locations of atmospheric DMS observations from cruise survey experiments 1-3, and the MSA observation site in Hua Niao Island.

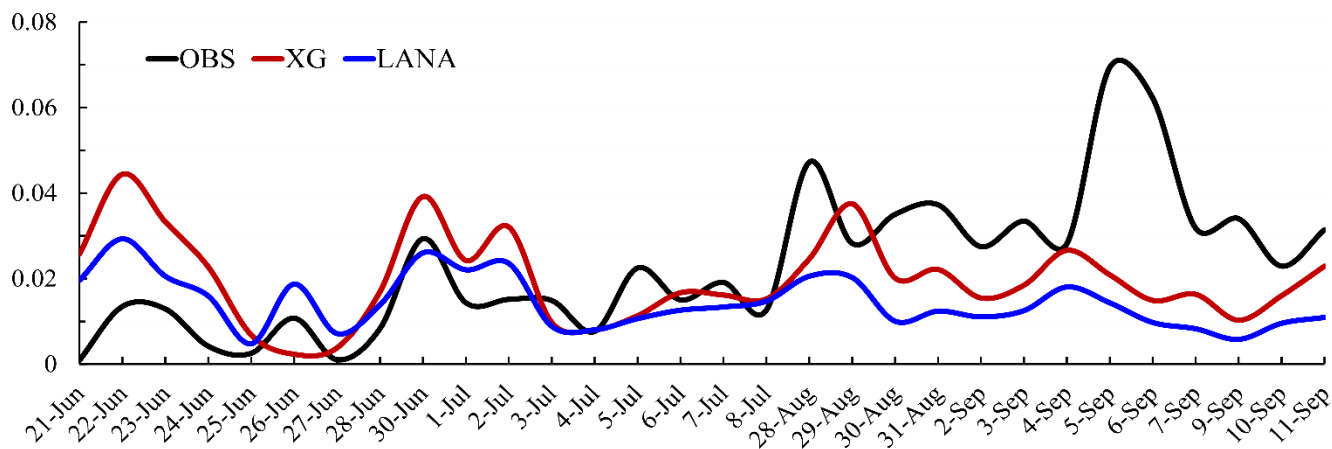


Figure 5. A comparison of simulated daily concentrations of MSA with observations at the Hua Niao Island site (Units: $\mu\text{g m}^{-3}$).

680



Absolute contribution of DMS to SO_4 (XG – ND)

DMS-derived DRF (XG – ND)

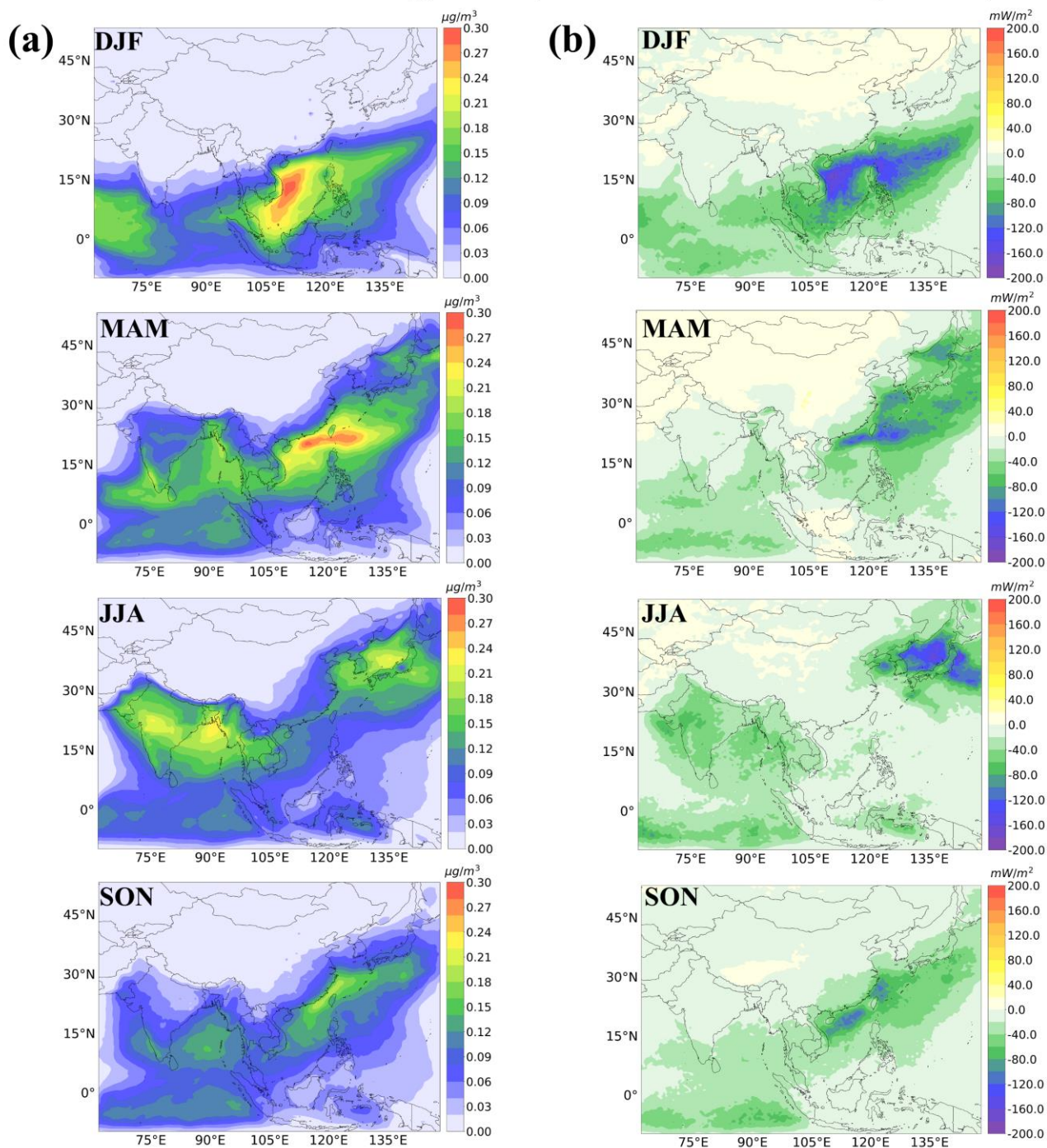
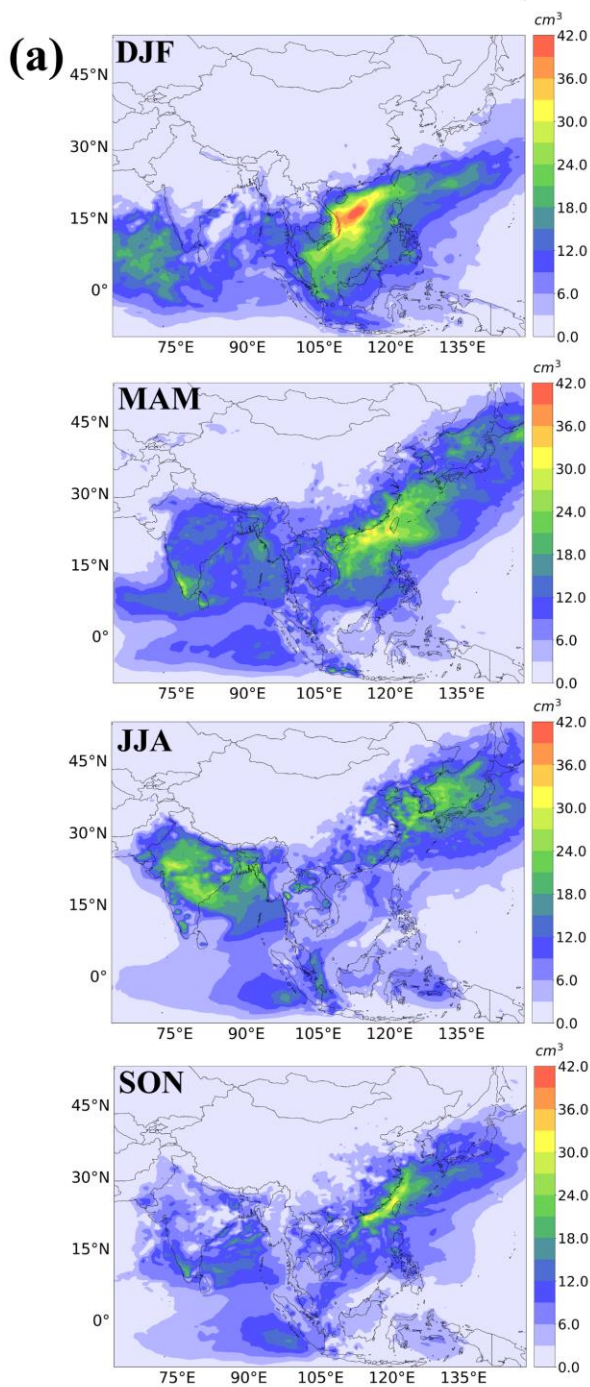


Figure 6. Spatial pattern of the seasonal mean absolute changes in surface SO_4^{2-} (first column) and all-sky DRF (second column) between the XG and ND (no DMS) simulations.



Absolute contribution of DMS to CCN (XG – ND)



DMS-derived IRF (XG – ND)

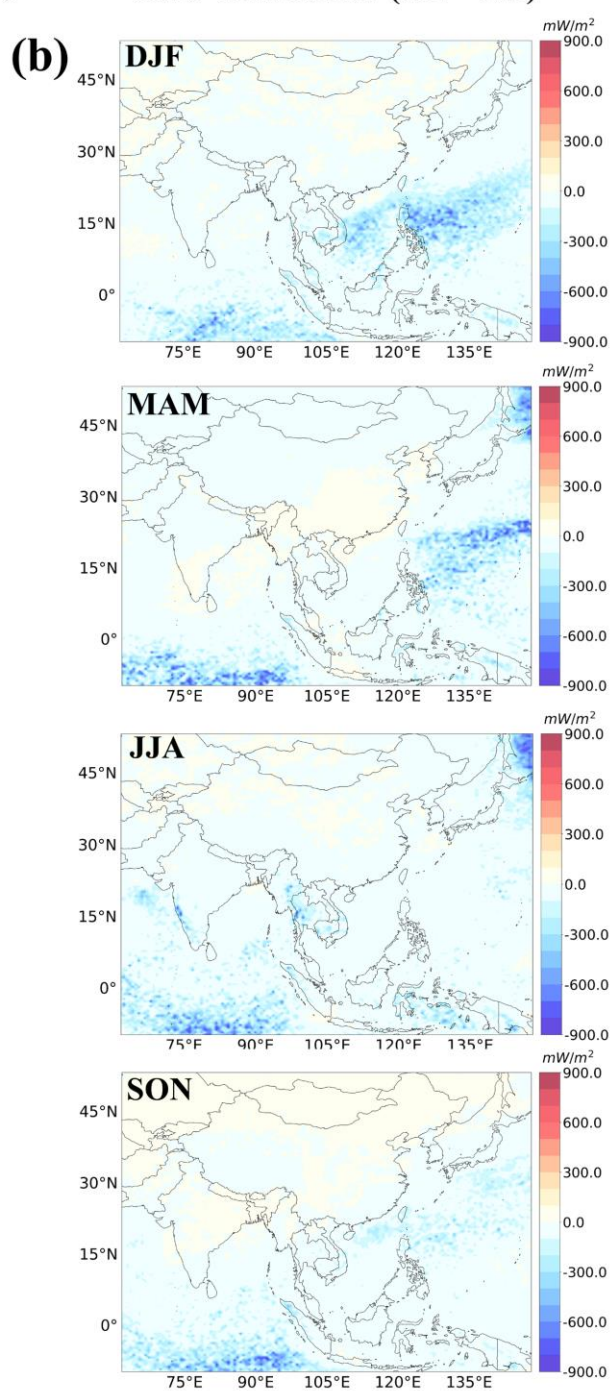
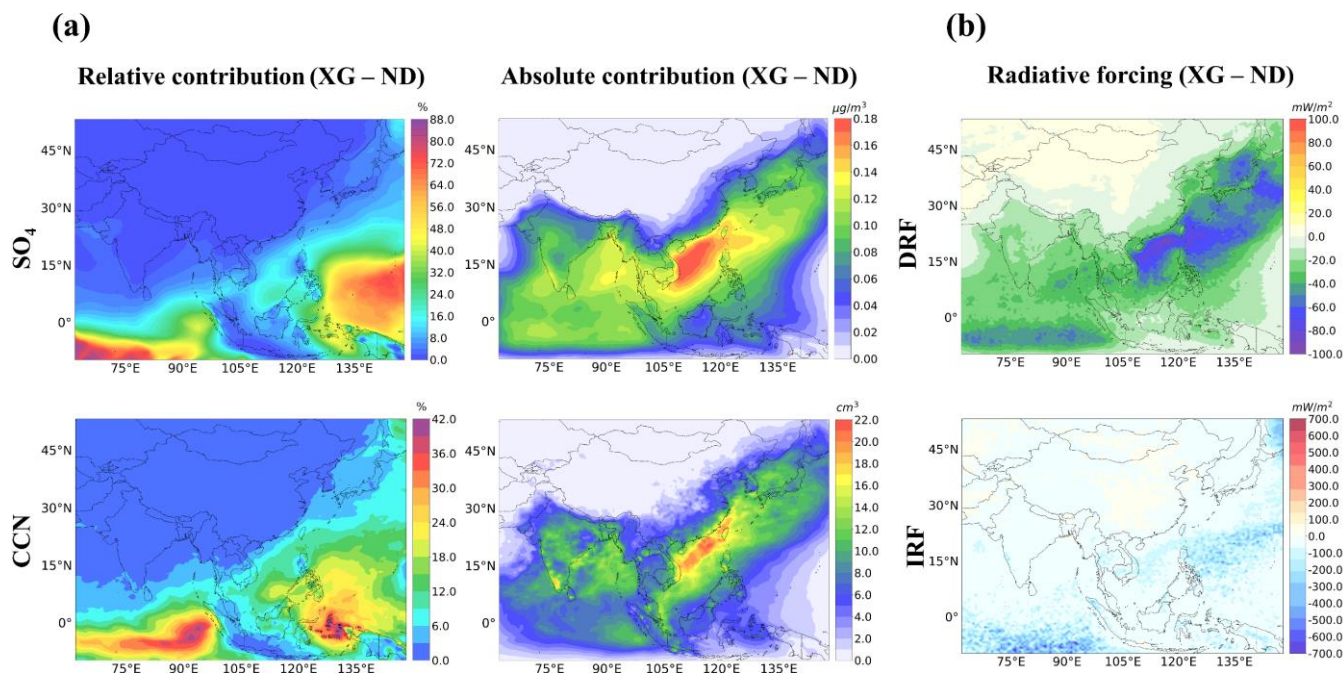




Figure 7. Spatial pattern of the seasonal mean absolute changes in surface CCN (0.2%) (first column) and cloud-albedo IRF (second column) between the XG and ND (no DMS) simulations.



690 **Figure 8.** Panel (a) presents the spatial distributions of annual mean percent changes and absolute changes in surface SO_4^{2-} and CCN, and panel (b) presents the spatial distributions of annual mean all-sky DRF and cloud-albedo IRF between XG and ND (no DMS) simulations.

Table 1. Description of simulation

Simulation	Description
XG	DMS emissions on with updated DMS emissions predicted by XGBoost model.
LANA	DMS emissions on with default DMS emissions from Lana et al. (2011).
ND	DMS emissions turned off.

695